Journal of Zhejiang University-SCIENCE A 2026 27(2):155-168
www.jzus.zju.edu.cn; www.springer.com/journal/11582
E-mail: jzus_a@zju.edu.cn

Research Article
https://doi.org/10.1631/jzus.A2500090

Check for updates

Axial compression performance and confinement mechanism of concrete-filled corrugated steel tubular columns

Jiaming ZHANG, Chaoqun YU, Genshu TONG, Jingzhong TONG✉

Institute of Advanced Engineering Structures, Zhejiang University, Hangzhou 310058, China

Abstract: The concrete-filled corrugated steel tubular (CFCST) column is a novel steel–concrete composite column characterized by transverse corrugated steel plates. This unique application of the plates leverages their considerable out-of-plane stiffness, markedly enhancing the compression performance of CFCST columns while significantly reducing steel material consumption. However, the exact confinement mechanism of the corrugated steel on the infilled concrete remains unclear. To address this question, we analyzed the confinement effect of the CFCST columns under axial compression. The lateral displacement, lateral stress, and bending moment distributions were determined through differential equations, and parametric analysis was performed to examine the impact of varying corrugated steel plate dimensions and concrete strength on these distributions. The results indicated strong confinement effects at the boundary positions, while virtually no effect at the mid-span. The stiffness of the corrugated steel plates and the confinement effect were found to be directly proportional. Additionally, a relationship was established between the average lateral stress of the concrete and the effective confinement coefficient of the CFCST through data fitting, leading to a design formula for calculating the axial compression capacity of CFCST columns. Finally, the accuracy of the formula and its applicability in engineering design were confirmed through validation on experimental data, with the maximum deviation being within ±5%.

Key words: Corrugated steel plate; Composite column; Confinement mechanism; Axial compressive behavior; Theoretical analysis

1 Introduction

In the field of structural engineering, the development of high-performance and easy-to-assemble structural forms has become a major trend. Steel–concrete composite structures, particularly concrete-filled steel tubular (CFST) columns, exemplify this with their extensive superior load-bearing capabilities and versatile design options, making them increasingly popular (Yu et al., 2024a). Since their first application in the Severn Railway Bridge in 1879, CFST columns have been widely used and studied due to their unique mechanical properties, which are driven by the synergistic interaction between the steel tube and infilled concrete (Han et al., 2014, 2016; Wang and Han, 2018; Hu and Liu, 2022). Numerous investigations have been conducted on constitutive models of confined concrete and revealed significant enhancements in both strength and ductility (Richart et al., 1928, 1929; Mander et al., 1988; Naguib and Mirmiran, 2003; Badalamenti et al., 2010; Yu et al., 2022). Additionally, extensive experimental and numerical studies have been conducted to investigate the load-bearing capacity of CFST columns under axial and eccentric compression (Furlong, 1967; Knowles and Park, 1969; Han and An, 2014). The axial performance of such columns can be improved either by replacing conventional concrete with high-performance cementitious composites, which typically exhibit superior crack resistance and durability (Gong et al., 2023; Chen et al., 2024; Tong et al., 2024b, 2025), or by enhancing the confinement effect of the outer steel tube on the core concrete. Due to their superior bending stiffness and ease of connection, rectangular CFST columns are widely employed in construction, although their confinement efficiency is weaker than that of circular CFST columns (Chen et al., 2025a, 2025b). The

✉ Jingzhong TONG, tongjz@zju.edu.cn
Jiaming ZHANG, https://orcid.org/0009-0007-9189-3172
Jingzhong TONG, https://orcid.org/0000-0003-3190-518X

Received Mar. 23, 2025; Revision accepted Sept. 8, 2025;
Crosschecked Dec. 25, 2025; Online first Jan. 21, 2026

wall plates of the rectangular steel tubes provide confinement mainly through bending resistance, but this mechanism is prone to premature buckling (Zhang et al., 2021a, 2021b; Zhang YJ et al., 2023). Conventional approaches, such as increasing the plate thickness or adding external stiffeners, can delay buckling but often result in higher construction complexity and material costs.

Instead, replacing flat plates with corrugated steel plates offers a more efficient solution. Despite being thin-walled, corrugated plates possess considerable bending stiffness due to their geometric configuration. They have already been applied in various practical engineering projects, which demonstrated their feasibility and effectiveness in enhancing both stiffness and structural stability (Tong et al., 2022, 2023b, 2023c; Wang et al., 2022; Wu et al., 2024). An example of corrugated steel plates in construction is shown in Fig. 1. Meanwhile, the bearing capacity and stability of some components using corrugated steel plates and filled concrete have been investigated (Wen et al., 2023; Dou et al., 2024; Jiang et al., 2024; Yu et al., 2024b; Wu et al., 2025). Some studies have confirmed that the mechanical interlocking between corrugated steel plates and infilled concrete enables better cooperative performance and effectively mitigates local buckling issues (Sun et al., 2022; Yu et al., 2023, 2025a; Zhang JW et al., 2023; Tong et al., 2024a, 2024c).

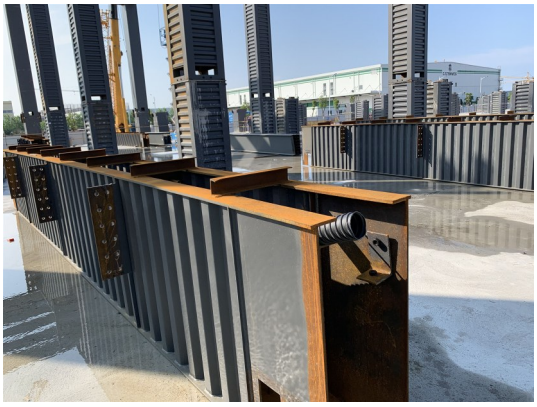

Fig. 1 Application of corrugated steel plates in practical engineering

Consequently, a novel structure named the concrete-filled corrugated steel tubular (CFCST) column has been proposed, which is depicted in Fig. 2. It consists of four transversely placed corrugated steel plates, four small square-section steel bars at the corners, and infilled concrete. The transverse corrugated plates can release axial loads in the vertical direction through the accordion effect, and their primary role is to provide circumferential confinement to the core concrete (Zhang et al., 2025). In contrast with vertically placed corrugated steel plates, this transverse configuration does not rely on the plates to directly carry axial loads, but it does effectively avoid premature buckling before the peak strength and ensures a higher residual capacity (Fang et al., 2022, 2023; Tong et al., 2023c; Yu et al., 2025b).

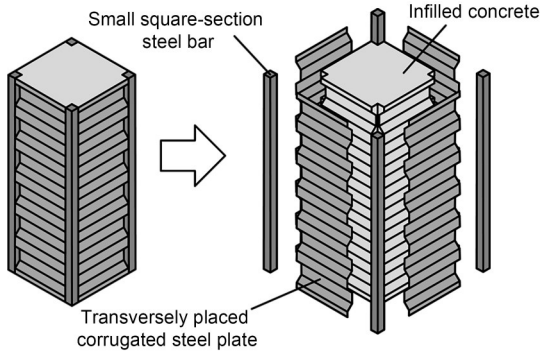

Fig. 2 Composition of a CFCST column

Additionally, due to their significant lateral bending stiffness, corrugated steel plates can effectively constrain the lateral expansion deformation of the infilled concrete. The small square-section steel bars placed at the corners of a CFCST column primarily serve to connect the corrugated steel plates to an integral cell through welding. Their dimensions are deliberately kept small—generally less than 1/10 of the column width—and are determined by constructability and economic considerations. This ensures that the steel bars are sufficiently large for reliable welding and assembly, while avoiding unnecessary material usage (Tong et al., 2024c). The welded corrugated cell can directly act as the formwork during concrete pouring, which makes the structure well-suited for modular construction. Compared with conventional CFST columns, CFCST columns provide enhanced confinement due to the boundary restraint offered by the corrugated plates. Moreover, corrugation allows for more efficient use of steel, leading to improved material economy without compromising structural performance. However, the axial bearing capacity of CFCST columns and the confinement mechanism exerted by the corrugated steel plates on the infilled concrete are not fully understood. Therefore, it is

imperative to investigate these aspects in order to advance the understanding and application of this innovative composite column.

In this study, the mechanical interaction between corrugated steel plates and infilled concrete in stub CFCST columns under axial loading is analyzed based on elastic theory. Differential equations were used to determine the lateral displacement, lateral stress, and bending moment distributions of the corrugated steel plates. Parameters such as the thickness, width, and amplitude of the steel plates, as well as the strength of the concrete, were examined to qualitatively assess their impact on the confinement effects and the confinement mechanism of the CFCST columns. Finally, methods for calculating average lateral stress and axial load-bearing capacity were developed and validated based on the existing experimental data, providing valuable guidance for their engineering applications.

2 Elastic mechanics analysis of the confinement effect

2.1 Simplified section

A previous experimental study (Tong et al., 2024c) demonstrated that for CFCST columns with horizontally placed corrugated plates, local buckling of these plates does not occur before the ultimate axial capacity is reached. In this stage, the plates are primarily bending, so it is reasonable to consider them as orthotropic plates. Under this assumption, the centroidal lines of the plates enclose an equivalent cross-section whose area coincides with the average of the maximum and minimum sectional areas. In addition, the confinement coefficient is calculated based on the volumetric ratio of steel to concrete, which is consistent with using the average section. Therefore, adopting the average section provides a rational simplification that aids mechanical analysis. In the design of the CFCST column, four steel bars with a square cross-section are strategically placed in each corner to connect the corrugated steel plates and bear the vertical load. Given that the area of the concrete invaded by the steel bars is small compared to the total cross-sectional area, this allows the cross-section to be treated as an intact rectangular section.

The simplified section is shown in Fig. 3, where $b_{c,max}$ and $h_{c,max}$ are the maximum width and height of the original section, respectively; $b_{c,min}$ and $h_{c,min}$ are the minimum width and height of the original section, respectively; b_c and h_c are the width and height of the simplified section, respectively. The cross-section of the corrugated steel plate is depicted in Fig. 4, where t is the plate thickness; a is the corrugation amplitude; γ is the inclined angle; d_1 and d_2 are the lengths of the horizontal and inclined segments, respectively; s and q are the unfolded length and projected length of one period of the corrugated steel plate, respectively. To distinguish the plates oriented in different directions, the two corrugated steel plates oriented along the width of the simplified section are designed as "flanges", whereas those oriented along the height of the simplified section are designed as "webs"—their related physical quantities are distinguished by the subscripts "f" and "w", respectively.

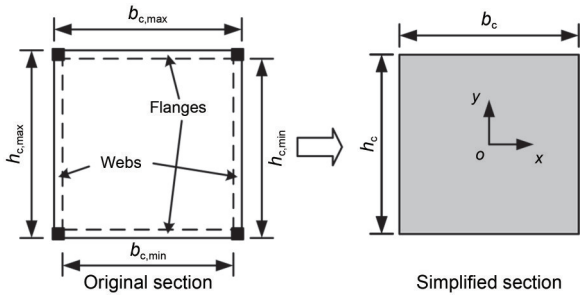

Fig. 3 Schematic diagram of the CFCST column section calculation

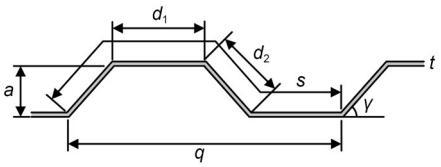

Fig. 4 Cross-section of a corrugated steel plate

2.2 Mechanism analysis based on elastic theory

Assuming that the CFCST column is uniformly compressed—that is, the axial compressive strain is consistent within any single cross-section—the rectangular coordinate system xoy is established with the center of the section as the origin. The compression direction is along the z-axis perpendicular to the xy plane, as shown in Fig. 3.

The elastic modulus and Poisson's ratio for concrete are denoted as E_c and μ_c, and those for steel are denoted as E and μ, respectively. At the initial stage, which involves slowly applying the axial load, the corrugated steel plate and the infilled concrete are considered to

bear the axial load independently. To facilitate the study of compression, both the stress and strain are considered as positive compression. Based on elastic theory and the equilibrium conditions of the corrugated steel plates, the bending equations in the two directions can be expressed as:

$$D_{\mathrm{w}}\frac{\mathrm{d}^4u}{\mathrm{d}y^4}+K_{\mathrm{w}}u=K_{\mathrm{w}}u^*, \tag{1}$$

$$D_{\mathrm{f}}\frac{\mathrm{d}^4v}{\mathrm{d}x^4}+K_{\mathrm{f}}v=K_{\mathrm{f}}v^*, \tag{2}$$

where x and y are the coordinates along the flange and web directions, respectively; u and v denote the displacement components in the x- and y-directions, respectively, and their positive directions align with those of the coordinate system; D_{w} and D_{f} are the bending stiffnesses of the web and flange, respectively. K_{w} and K_{f} are the equivalent constraint stiffness parameters; u^* and v^* are the equivalent displacement parameters.

The complete derivation of the above equations is presented in Eqs. (S1)–(S33) of the electronic supplementary materials (ESM). Accordingly, Eqs. (3) and (4) are the solutions of Eqs. (1) and (2), respectively:

$$\begin{aligned}u=0.5\varepsilon_{\mathrm{c}_z}b_{\mathrm{c}}[&A_{\mathrm{w}_0}\sinh(k_{\mathrm{w}}y)\sin(k_{\mathrm{w}}y)+\\&C_{\mathrm{w}_0}\cosh(k_{\mathrm{w}}y)\cos(k_{\mathrm{w}}y)]+u^*,\end{aligned} \tag{3}$$

$$\begin{aligned}v=0.5\varepsilon_{\mathrm{c}_z}h_{\mathrm{c}}[&A_{\mathrm{f}_0}\sinh(k_{\mathrm{f}}x)\sin(k_{\mathrm{f}}x)+\\&C_{\mathrm{f}_0}\cosh(k_{\mathrm{f}}x)\cos(k_{\mathrm{f}}x)]+v^*,\end{aligned} \tag{4}$$

where $k_{\mathrm{w}}=\sqrt[4]{K_{\mathrm{w}}/(4D_{\mathrm{w}})}$ and $k_{\mathrm{f}}=\sqrt[4]{K_{\mathrm{f}}/(4D_{\mathrm{f}})}$ denote characteristic parameters reflecting the relative stiffness between the equivalent constraint stiffness and the bending stiffness; $\varepsilon_{\mathrm{c}_z}$ is the axial strain; A_{w_0}, A_{f_0}, C_{w_0}, and C_{f_0} are undetermined constants. The detailed calculation methods are provided in Eqs. (S47)–(S50) of the ESM.

The lateral stresses in the x- and y-directions, p_x and p_y, between the corrugated steel plates and the infilled concrete are:

$$\begin{aligned}p_x=-0.5\varepsilon_{\mathrm{c}_z}b_{\mathrm{c}}K_{\mathrm{w}}[&A_{\mathrm{w}_0}\sinh(k_{\mathrm{w}}y)\sin(k_{\mathrm{w}}y)+\\&C_{\mathrm{w}_0}\cosh(k_{\mathrm{w}}y)\cos(k_{\mathrm{w}}y)],\end{aligned} \tag{5}$$

$$\begin{aligned}p_y=-0.5\varepsilon_{\mathrm{c}_z}h_{\mathrm{c}}K_{\mathrm{f}}[&A_{\mathrm{f}_0}\sinh(k_{\mathrm{f}}x)\sin(k_{\mathrm{f}}x)+\\&C_{\mathrm{f}_0}\cosh(k_{\mathrm{f}}x)\cos(k_{\mathrm{f}}x)].\end{aligned} \tag{6}$$

The tensile forces T_{w} and T_{f} acting on the web and flange are then:

$$\begin{aligned}T_{\mathrm{w}}=-\frac{K_{\mathrm{f}}h_{\mathrm{c}}\varepsilon_{\mathrm{c}_z}}{4k_{\mathrm{f}}}[&A_{\mathrm{f}_0}(\cosh U_{\mathrm{f}}\sin U_{\mathrm{f}}-\sinh U_{\mathrm{f}}\cos U_{\mathrm{f}})+\\&C_{\mathrm{f}_0}(\sinh U_{\mathrm{f}}\cos U_{\mathrm{f}}+\cosh U_{\mathrm{f}}\sin U_{\mathrm{f}})],\end{aligned} \tag{7}$$

$$\begin{aligned}T_{\mathrm{f}}=-\frac{K_{\mathrm{w}}b_{\mathrm{c}}\varepsilon_{\mathrm{c}_z}}{4k_{\mathrm{w}}}[&A_{\mathrm{w}_0}(\cosh U_{\mathrm{w}}\sin U_{\mathrm{w}}-\sinh U_{\mathrm{w}}\cos U_{\mathrm{w}})+\\&C_{\mathrm{w}_0}(\sinh U_{\mathrm{w}}\cos U_{\mathrm{w}}+\cosh U_{\mathrm{w}}\sin U_{\mathrm{w}})],\end{aligned} \tag{8}$$

where $U_{\mathrm{w}}=0.5k_{\mathrm{w}}h_{\mathrm{c}}$ and $U_{\mathrm{f}}=0.5k_{\mathrm{f}}b_{\mathrm{c}}$, and the two are dimensionless characteristic parameters governing the deformation distribution along the web and flange directions, respectively.

With this result, the solutions for all the physical quantities have been obtained. Given that local buckling of the corrugated steel plates generally does not occur prior to significant expansion of the infilled concrete, the preceding analysis based on elastic theory is considered reasonable.

3 Parameter analysis of the confinement mechanism

3.1 Lateral displacement distribution

To simplify the analysis, we only consider the case of a biaxial symmetric section, where all the parameters have equal corresponding values in the x- and y-directions. At the initial stage of loading, the interaction between the corrugated steel plates and the infilled concrete is weak, and it can be assumed that these bodies are independently subjected to stress without interacting. Under these conditions, the displacement in the y-direction v_{c_0} at the boundary of the concrete due to axial compression is:

$$v_{\mathrm{c}_0}=0.5\mu_{\mathrm{c}}\varepsilon_{\mathrm{c}_z}h_{\mathrm{c}}. \tag{9}$$

The confinement effect of the corrugated steel plates on the infilled concrete can be evaluated by comparing Eqs. (4) and (9):

$$\frac{v}{v_{c_0}}=\frac{1}{\mu_c}[A_{f_0}\sinh(k_f x)\sin(k_f x)+C_{f_0}\cosh(k_f x)\cos(k_f x)]+\frac{v^*}{v_{c_0}}, \tag{10}$$

$$\frac{v^*}{v_{c_0}}=1-(A_{w_0}\sinh U_w \sin U_w + C_{w_0}\cosh U_w \cos U_w). \tag{11}$$

Notably, concrete is a typical nonlinear material, and its Poisson's ratio should be taken as the secant Poisson's ratio, which increases gradually during loading. The elastic modulus should be considered as the secant modulus, which tends to decrease simultaneously. The relationship between the secant modulus and the tangent modulus at the origin for concrete is difficult to ascertain, but employing the tangent modulus at the origin as the elastic modulus does not affect the qualitative conclusions. The tangent modulus at the origin is calculated by Eq. (12) (ACI, 2019):

$$E_c=4733\sqrt{f_c'}, \tag{12}$$

where f_c' is the compressive strength of a 150 mm×300 mm cylinder of concrete.

Based on Eqs. (9)–(11), the function curves can be plotted as shown in Fig. 5. Due to symmetry, only the function curves in the first quadrant are shown. The ratio of lateral displacement in the y-direction between the corrugated steel plate and the unconfined concrete reflects the confinement effect. At the position near the boundary (when x approaches $0.5b_c$), the lateral displacement of the corrugated steel plate is smaller than that of the unconfined concrete, indicating that the corrugated steel plate provides strong confinement to the infilled concrete in this location. Conversely, at the position near the mid-span of the corrugated steel plate (when x approaches 0), the lateral displacement of the corrugated steel plate is even greater than that of the unconfined concrete, indicating that the confinement effect here is very weak; it may even indicate that the

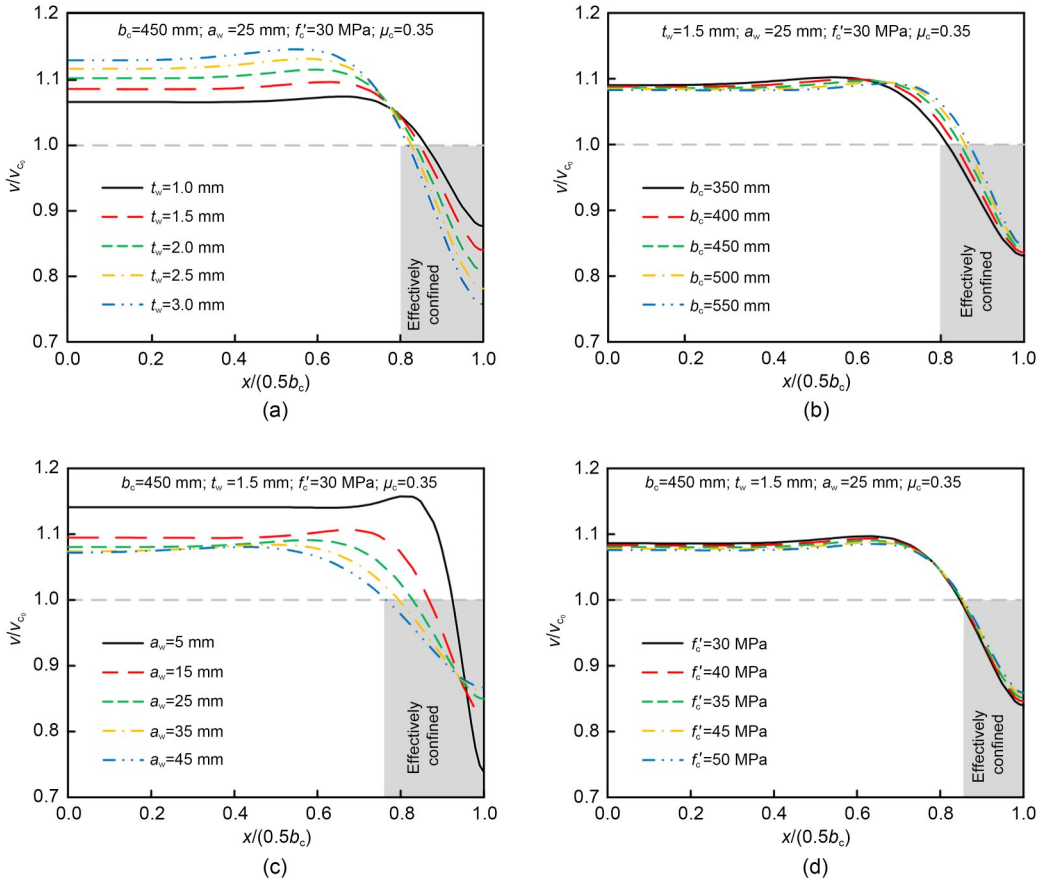

Fig. 5 Lateral displacement distributions for different parameters: (a) thickness of the web; (b) width of the simplified section; (c) amplitude of the web; (d) compressive strength of the concrete

corrugated steel plate and the infilled concrete become detached.

As shown in Fig. 5a, an increase in the thickness of the web t_w makes this phenomenon more pronounced, and when t_w approaches 0, the function curve approaches the line $v/v_{c_0}=1$, which indicates that the infilled concrete has become unconfined. As the width of the simplified section b_c increases, the effective confinement area decreases, as illustrated in Fig. 5b. Meanwhile, looking at Fig. 5c, an increase in the amplitude of the web a_w significantly enlarges the effective confinement area. In general, the distribution of lateral displacement is closely related to the bending stiffness of the corrugated steel plate, and greater stiffness results in a better confinement effect. Therefore, the compressive strength of the materials does not directly affect the distribution of lateral displacement. As depicted in Fig. 5d, the lateral displacement distribution curves of CFCST columns with different compressive strengths f_c' are almost identical, with only minor variations occurring due to the relationship between the elastic modulus and the compressive strength of the concrete, as described by Eq. (12). Additionally, this indicates that the impact of the elastic modulus of the concrete on the calculation results can be considered as negligible.

3.2 Lateral stress distribution and confinement coefficient

The lateral stress on the surface of the infilled concrete can be calculated by Eqs. (5) and (6). At the corner points of the concrete, the lateral stress is maximal, and the maximal lateral stress $p_{y,\max}$ is given by:

$$p_{y,\max}=-\frac{(1-\mu_c)E_c\varepsilon_{c_z}}{(1+\mu_c)(1-2\mu_c)}(A_{f_0}\sinh U_f\sin U_f+C_{f_0}\cosh U_f\cos U_f). \tag{13}$$

To facilitate our analysis, we express the lateral stress between the corrugated steel plate and the infilled concrete under collaborative working conditions in dimensionless form as:

$$\frac{p_y}{p_{c_0}}=-\frac{1-\mu_c}{\mu_c(1+\mu_c)(1-2\mu_c)}[A_{f_0}\sinh(k_f x)\sin(k_f x)+C_{f_0}\cosh(k_f x)\cos(k_f x)], \tag{14}$$

$$p_{c_0}=\mu_c E_c\varepsilon_{c_z}, \tag{15}$$

where p_{c_0} is the reference lateral stress of the infilled concrete induced by the Poisson effect under axial compression.

Based on Eq. (14), the lateral stress distribution curves are calculated and shown in Fig. 6. The lateral stress is maximal at the boundary position and approaches 0 at the mid-span. The distribution curves are approximately linear near the boundary. As the thickness of the web t_w increases, the lateral stress also increases, as pictured in Fig. 6a. Conversely, as the width of the simplified section b_c increases, the lateral stress decreases, as depicted in Fig. 6b. It should be noted that when the amplitude of the web a_w increases, the maximum value of the lateral stress decreases, and the position where the lateral stress diminishes to 0 moves further from the boundary, as observed in Fig. 6c. Similarly, the compressive strength of the concrete material f_c' does not directly affect the distribution of lateral stress, but instead influences it indirectly through stiffness; as the stiffness of the concrete increases, the lateral stress slightly decreases, as shown in Fig. 6d.

Based on the analysis above, the lateral stress near the boundary can be simplified as a linear distribution, with a schematic diagram of this calculation shown in Fig. 7. The single-sided equivalent bearing width $b_{c,e}$ of the corrugated steel plate during the elastic phase can be defined and calculated as:

$$b_{c,e}=\frac{2T_w}{p_{y,\max}}=4\sqrt[4]{\frac{D_f}{4K_f}}\frac{\cosh(2U_f)-\cos(2U_f)}{\sinh(2U_f)+\sin(2U_f)}. \tag{16}$$

Since U_f is a large value ($U_f\approx 8$), both $\cosh(2U_f)$ and $\sinh(2U_f)$ reach values on the order of 10^6, which are far greater than the bounded trigonometric terms. As a result, the part of the equation involving trigonometric and hyperbolic functions approaches 1, and Eq. (16) can be further simplified as:

$$b_{c,e}=\frac{2}{k_f}=2\sqrt[4]{\frac{(1+\mu_c)(1-2\mu_c)\left(d_{f_1}+\frac{d_{f_2}}{3\cos\gamma_f}\right)Et_f a_f^2 h_c}{(1-\mu_c)E_c q_f}}, \tag{17}$$

where d_{f_1}, d_{f_2}, γ_f, t_f, a_f, and q_f are the geometric parameters of the corrugated steel plate used as the flange,

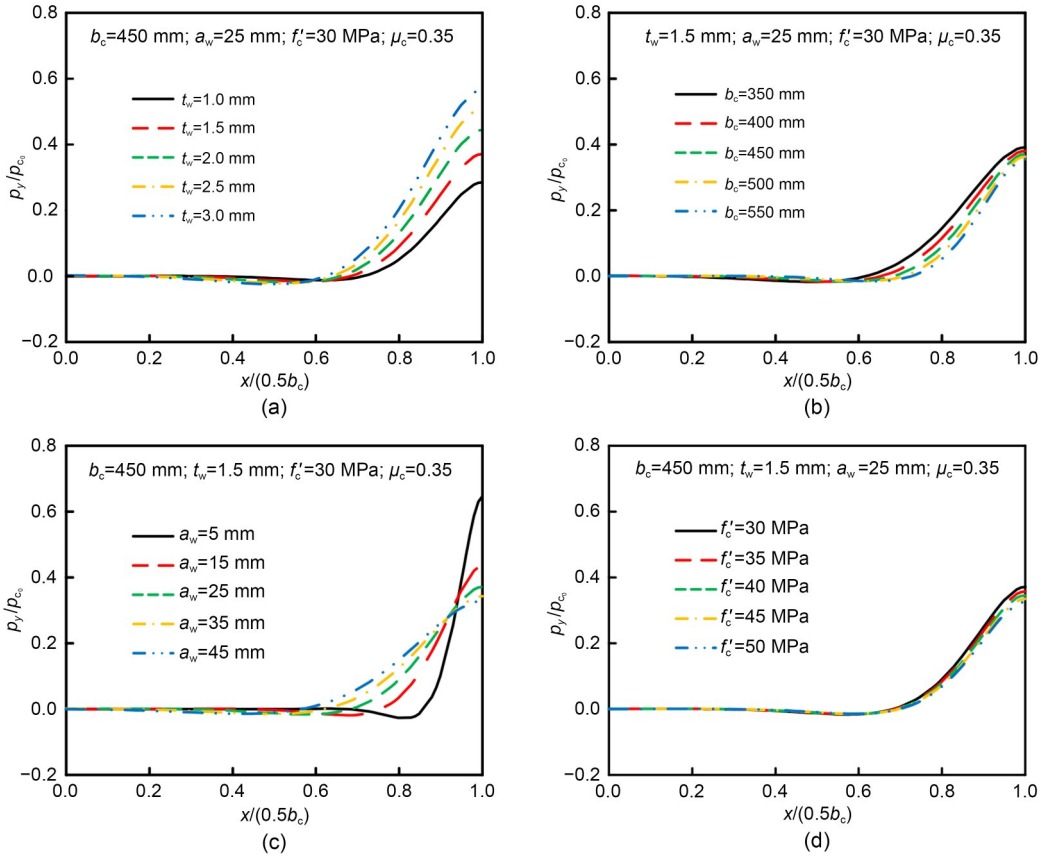

Fig. 6 Lateral stress distributions with different parameters: (a) thickness of the web; (b) width of the simplified section; (c) amplitude of the web; (d) compressive strength of the concrete

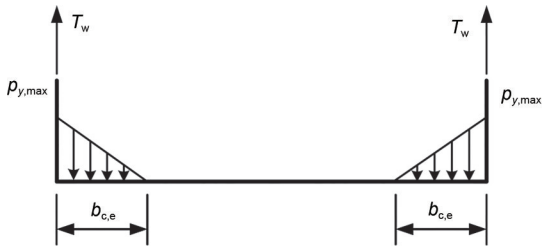

Fig. 7 Simplified distribution of the lateral stress and equivalent width of the area experiencing compression

and they have the same meaning as the variables shown in Fig. 4.

In the design of CFCST columns, the lateral stress in the infilled concrete is of critical importance when the column reaches the peak axial load. Therefore, we propose a simple method to estimate the stress at this state. Due to the significant variation in lateral stress along the span of the corrugated steel plate, the average stress $p_{y,\mathrm{avg}}$ can be used for a simple estimation. The tensile forces in the corrugated steel plates can be calculated by Eqs. (7) and (8), and the average stress between the corrugated steel plate and the infilled concrete can be defined as:

$$p_{y,\mathrm{avg}}=\frac{T_{\mathrm{w}}}{0.5b_{\mathrm{c}}}. \tag{18}$$

Similar to Eq. (14), the dimensionless form of the average lateral stress can be expressed as:

$$\begin{aligned}\frac{p_{y,\mathrm{avg}}}{p_{c_0}}=&-\frac{1-\mu_{\mathrm{c}}}{\mu_{\mathrm{c}}(1+\mu_{\mathrm{c}})(1-2\mu_{\mathrm{c}})}\frac{1}{2U_{\mathrm{f}}}\times\\&[A_{\mathrm{f}_0}(\cosh U_{\mathrm{f}}\sin U_{\mathrm{f}}-\sinh U_{\mathrm{f}}\cos U_{\mathrm{f}})+\\&C_{\mathrm{f}_0}(\sinh U_{\mathrm{f}}\cos U_{\mathrm{f}}+\cosh U_{\mathrm{f}}\sin U_{\mathrm{f}})].\end{aligned} \tag{19}$$

During compression, the apparent Poisson's ratio of the concrete increases with the development of lateral dilation and may approach 0.5 near the peak stress. We consider that to account for the observed nonlinear behavior of concrete (Tian et al., 2025). Additionally, in confined concrete structures, a confinement

coefficient is commonly used to simply evaluate the confinement effect. For CFCST columns with biaxial symmetric cross-sections, the confinement coefficient θ can be defined as:

$$\theta=\alpha_{\mathrm{s,e}}\frac{f_{\mathrm{y,p}}}{f_{\mathrm{c}}'}, \tag{20}$$

$$\alpha_{\mathrm{s,e}}=\frac{A_{\mathrm{s,p}}\dfrac{s}{q}}{A_{\mathrm{c,avg}}}=\frac{4t_{\mathrm{f}}}{b_{\mathrm{c}}+a_{\mathrm{f}}}\frac{s_{\mathrm{f}}}{q_{\mathrm{f}}}, \tag{21}$$

where $\alpha_{\mathrm{s,e}}$ is the effective steel ratio—this parameter represents the efficiency of the corrugated plates in providing confinement to the core concrete, where the contribution of the corner steel bars is negligible and thus excluded from the definition; $f_{\mathrm{y,p}}$ is the yield strength of the corrugated steel plates; $A_{\mathrm{s,p}}$ is the total cross-sectional area of the four corrugated steel plates; $A_{\mathrm{c,avg}}$ is the calculated area of the infilled concrete, taken as the average area; s_{f} is the unfolded length of one period of the corrugated steel plate used as the flange.

The preceding analysis indicates that the lateral stress is related to stiffness, but not directly to the material strength. Therefore, fitting can be performed between the average lateral stress and the effective steel ratio. The selected parameters and ranges for this fitting are: t_{w} from 1.0 to 3.0 mm with a step of 0.5 mm; b_{c} from 300 to 600 mm with a step of 50 mm; a_{w} from 5 to 45 mm with a step of 10 mm. Based on physical significance, the intercept of the function is defined as 0. The fitting results, illustrated in Fig. 8, can be concisely represented by a linear function:

$$\frac{p_{\mathrm{y,avg}}}{p_{\mathrm{c_0}}}=3.7\alpha_{\mathrm{s,e}}. \tag{22}$$

Furthermore, the corrugated steel plate could fail if the tensile force exceeds its ultimate tensile strength $T_{\mathrm{f,cr_0}}$. Therefore, it is necessary to validate the following formula with:

$$T_{\mathrm{f}}<T_{\mathrm{f,cr_0}}=t_{\mathrm{f}}\frac{s_{\mathrm{f}}}{q_{\mathrm{f}}}f_{\mathrm{y,p}}. \tag{23}$$

By incorporating Eqs. (18) and (22), Eq. (23) can be further simplified as:

$$\frac{a_{\mathrm{f}}}{b_{\mathrm{c}}}>\frac{3.7E_{\mathrm{c}}\varepsilon_{\mathrm{c_z}}}{f_{\mathrm{y,p}}}-1. \tag{24}$$

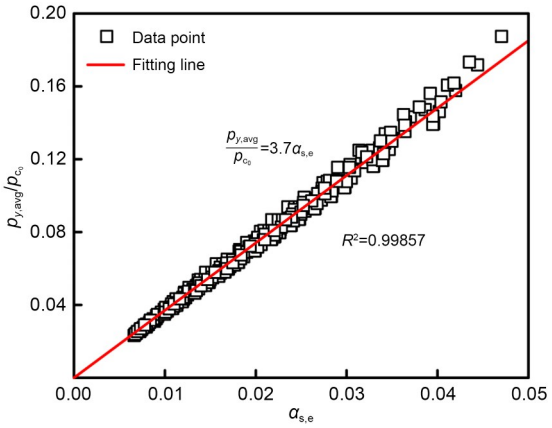

Fig. 8 Linear relationship between average lateral pressure and effective steel ratio. R^2 is the coefficient of correlation

Using Eq. (24), it is possible to select the specifications and strength of the corrugated steel plates used in CFCST columns or to verify the parameters of existing CFCST column cross-sections. When $f_{\mathrm{y,p}}$ is greater than or equal to $3.7E_{\mathrm{c}}\varepsilon_{\mathrm{c_z}}$ (which is in most cases), Eq. (24) holds true. If this condition is not satisfied, the corrugated steel plates may fail before the infilled concrete reaches its peak load capacity, resulting in a premature failure of the structure. In such cases, the strength of both the steel and the concrete, as well as the confinement effect, cannot be fully utilized, and the design is therefore considered unreasonable.

3.3 Lateral bending moment distribution

When the CFCST column is subjected to axial compression, the corrugated steel plates are in a state of tension and bending. The lateral bending moment M_y and its dimensionless form can be presented as:

$$M_y=-D_{\mathrm{f}}v''=-D_{\mathrm{f}}\varepsilon_{\mathrm{c_z}}h_{\mathrm{c}}k_{\mathrm{f}}^2[A_{\mathrm{f_0}}\cosh(k_{\mathrm{f}}x)\cos(k_{\mathrm{f}}x)-C_{\mathrm{f_0}}\sinh(k_{\mathrm{f}}x)\sin(k_{\mathrm{f}}x)], \tag{25}$$

$$\frac{M_y}{M_{\mathrm{c_0}}}=-\frac{100(1-\mu_{\mathrm{c}})}{\mu_{\mathrm{c}}(1+\mu_{\mathrm{c}})(1-2\mu_{\mathrm{c}})}\frac{1}{U_{\mathrm{f}}^2}\times[A_{\mathrm{f_0}}\cosh(k_{\mathrm{f}}x)\cos(k_{\mathrm{f}}x)-C_{\mathrm{f_0}}\sinh(k_{\mathrm{f}}x)\sin(k_{\mathrm{f}}x)], \tag{26}$$

$$M_{\mathrm{c_0}}=\frac{1}{800}\mu_{\mathrm{c}}E_{\mathrm{c}}\varepsilon_{\mathrm{c_z}}b_{\mathrm{c}}^2, \tag{27}$$

where v'' is the second derivative of the displacement v with respect to x; $M_{\mathrm{c_0}}$ is the reference bending moment adopted for normalization.

The bending moment distribution of the corrugated steel plate, as illustrated in Fig. 9 and calculated from Eq. (26), shows that the moment is 0 at the mid-span of the plate, and increases until reaching the maximum positive value $M_{y,\max}$, and then shifts to achieve the maximum negative value $M_{y,\min}$ at the boundary. Notably, the absolute value of the maximum negative moment $|M_{y,\min}|$ is approximately 4.812 times that of the maximum positive moment $|M_{y,\max}|$.

As the thickness t_w and amplitude a_w of the web increase, the absolute values of both the maximum positive and negative moments increase, and the location of the maximum positive moment moves further away from the boundary, as shown in Figs. 9a and 9c. Conversely, as the width of the simplified section b_c and the compressive strength of the concrete f_c' increase, the absolute values of both the maximum positive and negative moments decrease, and the location of the maximum positive moment moves closer to the boundary, as illustrated in Figs. 9b and 9d. In other words, the stiffness ratio of the corrugated steel plate to the infilled concrete per unit width controls the position of $M_{y,\max}$: a higher ratio moves it away from the boundary, whereas a lower ratio moves it closer to the boundary.

When the CFCST column is axially compressed, the corrugated steel plates are subjected to lateral stress due to the confinement effect, as well as normal stress along their width direction. Given these distinctive stress characteristics, the corrugated steel plate can be considered as a beam that is fixed at both ends, as depicted in Fig. 10a. With increasing load, negative moment plastic hinges first form at the supports, and then the beam behaves like a structure that is hinged at both ends, as shown in Fig. 10b. This continues until positive moment plastic hinges form at two symmetrical points around the mid-span, at which point the structure becomes unsuitable for bearing additional loads, as illustrated in Fig. 10c.

At the elastic limit state, the maximum bending moment M_e occurs at the supports and can be calculated as:

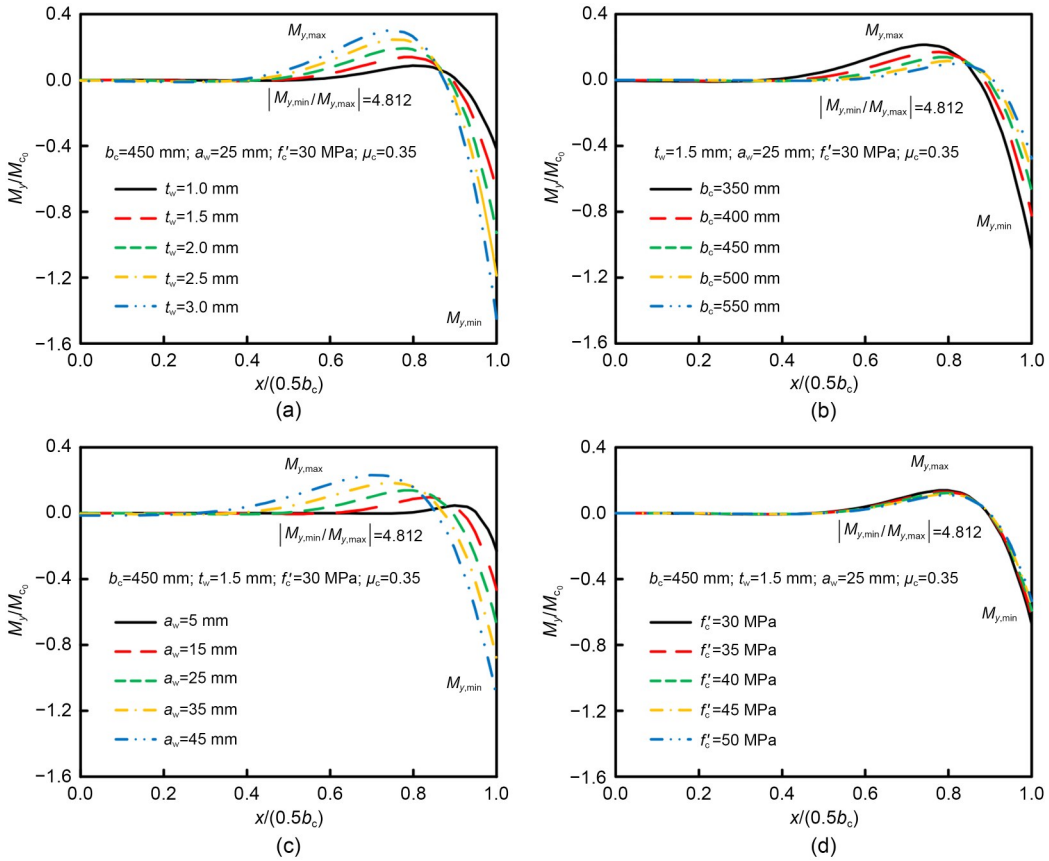

Fig. 9 Lateral bending moment distributions with different parameters: (a) thickness of the web; (b) width of the simplified section; (c) amplitude of the web; (d) compressive strength of the concrete

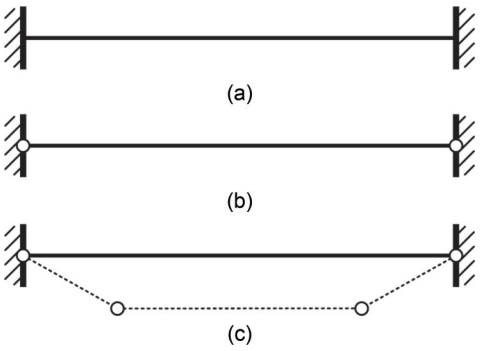

Fig. 10 Failure process of the corrugated steel plate: (a) initial state; (b) elastic limit state; (c) plastic limit state

$$M_{\mathrm{e}}=\left(\frac{1}{6}-\frac{b_{\mathrm{c,e}}}{9b_{\mathrm{c}}}\right)p_{\mathrm{y,max}}b_{\mathrm{c,e}}^{2}=2\left(\frac{1}{6}-\frac{b_{\mathrm{c,e}}}{9b_{\mathrm{c}}}\right)T_{\mathrm{w}}b_{\mathrm{c,e}}. \quad (28)$$

After the formation of negative moment plastic hinges, the location of the maximum positive moment approaches the mid-span of the corrugated steel plate, culminating in a plastic limit state.

4 Axial compression capacity of CFCST columns

Since CFCST columns are composite components with a low steel ratio, and the corrugated steel plates cannot directly bear the axial load due to an "accordion effect", the axial compression capacity is primarily determined by the infilled concrete. It can be inferred that the axial load-strain curves of CFCST columns should synchronize with that of the infilled concrete. When the infilled concrete reaches its peak compressive strain, the CFCST column attains its axial compression capacity. Based on the results and data fitting of Han et al. (2016), the peak axial compressive strain for CFCST columns can be calculated as:

$$\varepsilon_{\mathrm{c}_z}=\frac{1300+12.5f_{\mathrm{c}}'+\left[1330+760\left(\frac{f_{\mathrm{c}}'}{24}-1\right)\right]\theta^{0.2}}{10^{6}}. \quad (29)$$

The transverse normal stress in the corrugated steel plate from tensile force can be calculated by Eq. (S44) of the ESM. Since the plate is in a unidirectional stress state, the yield criterion σ_{c_y} is:

$$\sigma_{\mathrm{c}_y}=f_{\mathrm{y,p}}. \quad (30)$$

The average lateral stress in the infilled concrete when the CFCST column reaches the peak load can be calculated by Eq. (22). According to Tong (2022), the relationship between the strength of infilled concrete $f_{\mathrm{c,p}}$ and its average lateral stress $p_{\mathrm{y,avg}}$ can be expressed as:

$$\frac{f_{\mathrm{c,p}}}{f_{\mathrm{c}}'}=1+2.603\left(\frac{p_{\mathrm{y,avg}}}{f_{\mathrm{c}}'}\right)^{0.81}. \quad (31)$$

The formula to calculate the axial compression capacity N_{u} of a CFCST column can then be derived:

$$N_{\mathrm{u}}=A_{\mathrm{s,bar}}f_{\mathrm{y,bar}}+A_{\mathrm{c,min}}f_{\mathrm{c,p}}, \quad (32)$$

$$f_{\mathrm{c,p}}=\left[1+4.284\left(\frac{E_{\mathrm{c}}\varepsilon_{\mathrm{c}_z}\alpha_{\mathrm{s,e}}}{f_{\mathrm{c}}'}\right)^{0.81}\right]f_{\mathrm{c}}', \quad (33)$$

where $A_{\mathrm{s,bar}}$ and $f_{\mathrm{y,bar}}$ are the total cross-sectional area and the yield strength of the four steel bars, respectively; $A_{\mathrm{c,min}}$ is the minimum cross-sectional area of the infilled concrete.

The results from the above analysis were compared with a previous experimental study (Tong et al., 2024c), as summarized in Table 1. The specimen labels denote the cross-sectional width, the width of the square steel bar, the type of corrugated steel plate (type A with a wave amplitude of 20 mm; type B with a wave amplitude of 35 mm), and the plate thickness. A total of 10 groups of specimens were tested, with each group containing two identical specimens, distinguished by the suffixes "-1" and "-2". The column height was taken as three times the cross-sectional width to eliminate potential global stability effects. All steel components were fabricated through automated mechanical processing to ensure high dimensional accuracy, and the geometric parameters adopted in the calculations were based on the actual measured dimensions, including initial imperfections. The concrete was cast in two separate batches, thereby introducing a degree of material variability and improving the representativeness of the testing program.

The loading and measurement setup for the tests is shown in Fig. 11a, and the failure mode of the corrugated steel plates is pictured in Fig. 11b. It can be observed that the corrugated steel plates exhibit an outward bending deformation under the compression of the infilled concrete, with significant deformation

Table 1 Comparison between the experimental and theoretical results

Specimen label	$f_{y,p}$ (MPa)	$f_{y,bar}$ (MPa)	f_c' (MPa)	b_c (mm)	θ	$N_{u,test}$ (kN)	N_u (kN)	$N_u/N_{u,test}$
C350-35-A1.5-1	506	341	36.35	317	0.324	5721	5670	0.99
C350-35-A1.5-2	506	341	36.35	317	0.324	5725	5670	0.99
C400-35-A1.5-1	506	341	36.35	367	0.284	7024	7003	1.00
C400-35-A1.5-2	506	341	36.35	367	0.284	6957	7003	1.01
C450-35-A1.5-1	506	341	36.35	417	0.253	8219	8477	1.03
C450-35-A1.5-2	506	341	36.35	417	0.253	8047	8477	1.05
C450-40-A1.5-1	506	385	36.35	417	0.247	9343	9251	0.99
C450-40-A1.5-2	506	385	36.35	417	0.247	9353	9251	0.99
C500-40-A1.5-1	506	385	40.33	467	0.206	12058	11708	0.97
C500-40-A1.5-2	506	385	40.33	467	0.206	12340	11708	0.95
C500-45-A1.5-1	506	360	40.33	467	0.202	12446	12130	0.97
C500-45-A1.5-2	506	360	40.33	467	0.202	12611	12130	0.96
C550-45-A1.5-1	506	360	40.33	517	0.185	14541	14123	0.97
C550-45-A1.5-2	506	360	40.33	517	0.185	14613	14123	0.97
C550-45-A2.0-1	466	360	40.33	516	0.227	14756	14706	1.00
C550-45-A2.0-2	466	360	40.33	516	0.227	14619	14706	1.01
C550-50-B1.5-1	498	384	40.33	502	0.201	14143	13891	0.98
C550-50-B1.5-2	498	384	40.33	502	0.201	14522	13891	0.96
C600-50-B1.5-1	498	384	40.33	552	0.184	16074	15969	0.97
C600-50-B1.5-2	498	384	40.33	552	0.184	16470	15969	0.99

$N_{u,test}$ is the peak axial bearing capacity obtained from the test

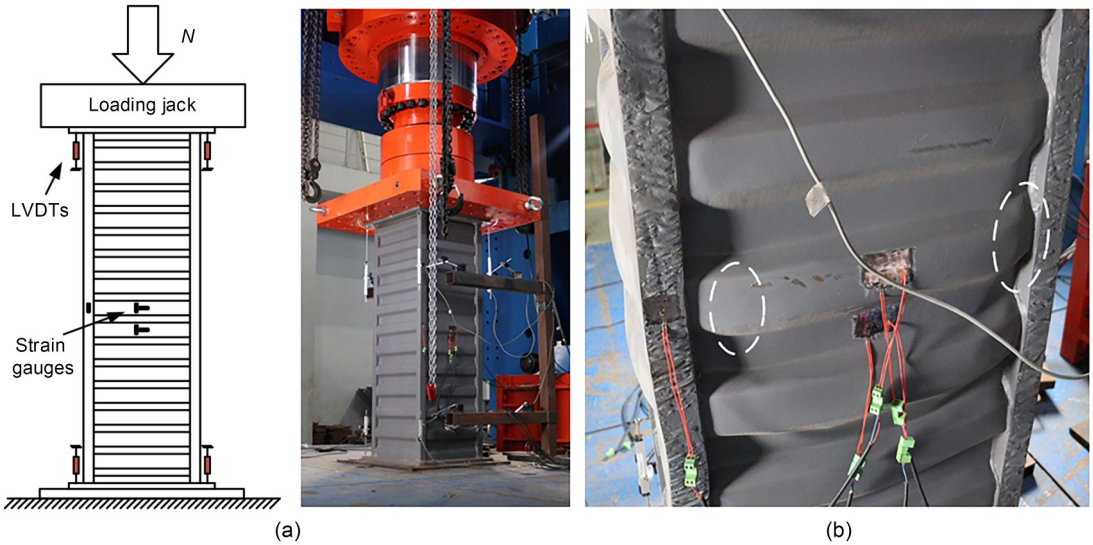

Fig. 11 (a) Axial compression test setup of CFCST columns; (b) failure mode of the corrugated steel plates. *N* is the applied axial compression; LVDT is the linear variable differential transformer

occurring near the ends. This is consistent with the failure mechanism shown in Fig. 10.

The peak axial bearing capacities obtained from the tests $N_{u,test}$, along with the calculated results from Eq. (32), are summarized in Table 1. The deviations between the theoretical and experimental results are within ±5%. Specifically, the mean value of $N_u/N_{u,test}$ is 0.99, with a standard deviation of 0.0243. In addition, regression analysis yields an R^2 value of 0.995, confirming that the proposed design formula provides

reliable prediction accuracy and is suitable for engineering applications.

5 Conclusions

CFCST columns are a new type of steel–concrete composite structure with a low steel ratio. The mechanical behavior of CFCST columns under axial compression was investigated analytically in this study.

Based on elastic theory, the interaction mechanism of corrugated steel plates with infilled concrete was derived from the relevant differential equations. This analysis covered the lateral displacement, stress, and bending moment of these components, providing a comprehensive assessment of their mechanical behavior under compressive loads.

The dimensions of the steel plates and the concrete strength were found to significantly influence lateral displacement, stress, and bending moment distributions. A substantial confinement effect was observed at the boundary positions, which was virtually absent at the mid-span. Increased flexural stiffness of the steel plates led to enhanced confinement and greater bending moments, with the peak negative bending moment being 4.812 times greater than the peak positive bending moment.

A method for calculating the effective steel ratio and confinement coefficient of CFCST columns was presented, and a simple linear relationship between the average lateral stress and the effective steel ratio at the peak load state was established. Furthermore, a formula for the axial compression capacity of CFCST columns was proposed and validated against experimental results. The maximum deviation from experimental data was less than ±5%, demonstrating the formula's high estimation accuracy and applicability for engineering design.

Acknowledgments

This work is supported by the Zhejiang Provincial Natural Science Foundation of China (No. LR24E080002) and the National Natural Science Foundation of China (Nos. 52522803 and 52478219).

Author contributions

Jiaming ZHANG designed the research and wrote the first draft of the manuscript. Chaoqun YU processed the corresponding data and helped to organize the manuscript. Genshu TONG and Jingzhong TONG revised and edited the final version.

Conflict of interest

Jiaming ZHANG, Chaoqun YU, Genshu TONG, and Jingzhong TONG declare that they have no conflict of interest.

References

ACI (American Concrete Institute), 2019. Building Code Requirements for Structural Concrete, ACI 318-19. ACI, Farmington Hills, USA.

Badalamenti V, Campione G, Mangiavillano ML, 2010. Simplified model for compressive behavior of concrete columns strengthened by steel angles and strips. *Journal of Engineering Mechanics*, 136(2):230-238. https://doi.org/10.1061/(asce)em.1943-7889.0000069

Chen YL, Tong JZ, Li QH, et al., 2024. Application of high-performance cementitious composites in steel–concrete composite bridge deck systems: a review. *Journal of Intelligent Construction*, 2(2):1-23. https://doi.org/10.26599/Jic.2024.9180012

Chen YL, Tong JZ, Li QH, et al., 2025a. Axial compressive tests and resistance design of UHTCC-encased rectangular steel tubular bridge columns. *Journal of Bridge Engineering*, 30(6):04025033. https://doi.org/10.1061/JBENF2.BEENG-7147

Chen YL, Tong JZ, Li QH, et al., 2025b. Local instability and interactive mechanism analysis of UHTCC-encased rectangular steel tubular columns. *Journal of Constructional Steel Research*, 228:109444. https://doi.org/10.1016/j.jcsr.2025.109444

Dou C, Ru Y, Jiang ZQ, et al., 2024. Lateral resistant behavior of grid-reinforced steel corrugated shear walls. *Journal of Structural Engineering*, 150(6):04024047. https://doi.org/10.1061/JSENDH.STENG-12285

Fang Y, Wang YY, Yang H, et al., 2022. Experimental behavior of concrete-filled thin-walled corrugated steel tubes with large helical angles under monotonic and cyclic axial compression. *Thin-Walled Structures*, 173:109043. https://doi.org/10.1016/j.tws.2022.109043

Fang Y, Wang YY, Yang LG, et al., 2023. Uniaxial monotonic and cyclic compressive stress–strain model for concrete-filled thin-walled helical corrugated steel tubes. *Journal of Structural Engineering*, 149(6):04023052. https://doi.org/10.1061/JSENDH.STENG-11719

Furlong RW, 1967. Strength of steel-encased concrete beam columns. *Journal of the Structural Division*, 93(5):113-124. https://doi.org/10.1061/JSDEAG.0001761

Gong FY, Sun XJ, Takahashi Y, et al., 2023. Computational modeling of combined frost damage and alkali-silica reaction on the durability and fatigue life of RC bridge decks. *Journal of Intelligent Construction*, 1(1):1-14. https://doi.org/10.26599/JIC.2023.9180001

Han LH, 2016. Concrete Filled Steel Tubular Structures—Theory and Practice. 3rd Edition. Science Press, Beijing, China (in Chinese).

Han LH, An YF, 2014. Performance of concrete-encased CFST stub columns under axial compression. *Journal of Constructional Steel Research*, 93:62-76. https://doi.org/10.1016/j.jcsr.2013.10.019

Han LH, Li W, Bjorhovde R, 2014. Developments and advanced applications of concrete-filled steel tubular (CFST) structures: members. *Journal of Constructional Steel Research*, 100:211-228. https://doi.org/10.1016/j.jcsr.2014.04.016

Han LH, Wang ZB, Xu W, et al., 2016. Behavior of concrete-encased CFST members under axial tension. *Journal of Structural Engineering*, 142(2):04015149. https://doi.org/10.1061/(asce)st.1943-541X.0001422

Hu B, Liu YY, 2022. Vehicular collision performance evaluation of concrete-filled steel tubular piers designed according to current codes in the US, Europe, and China. *Journal of Bridge Engineering*, 27(6):04022038. https://doi.org/10.1061/(asce)be.1943-5592.0001889

Jiang ZQ, Niu ZY, Zhang AL, et al., 2024. Design method of axial compression stability for cross-section corrugated plate steel special-shaped column. *Thin-Walled Structures*, 194:111243. https://doi.org/10.1016/j.tws.2023.111243

Knowles RB, Park R, 1969. Strength of concrete filled steel tubular columns. *Journal of the Structural Division*, 95(12):2565-2588. https://doi.org/10.1061/JSDEAG.0002425

Mander JB, Priestley MJN, Park R, 1988. Theoretical stress-strain model for confined concrete. *Journal of Structural Engineering*, 114(8):1804-1826. https://doi.org/10.1061/(asce)0733-9445(1988)114:8(1804)

Naguib W, Mirmiran A, 2003. Creep analysis of axially loaded fiber reinforced polymer-confined concrete columns. *Journal of Engineering Mechanics*, 129(11):1308-1319. https://doi.org/10.1061/(asce)0733-9399(2003)129:11(1308)

Richart FE, Brandtzæg A, Brown RL, 1928. A Study of the Failure of Concrete Under Combined Compressive Stresses. Technical Report No. 185, Engineering Experimental Station, University of Illinois, Urbana, USA.

Richart FE, Brandtzæg A, Brown RL, 1929. The Failure of Plain and Spirally Reinforced Concrete in Compression. Technical Report No. 190, Engineering Experimental Station, University of Illinois, Urbana, USA.

Sun ZX, Zou Y, Wang CQ, et al., 2022. Study on confinement mechanism of core concrete in steel tubular-corrugated steel plate confined concrete columns. *Journal of Building Engineering*, 52:104497. https://doi.org/10.1016/j.jobe.2022.104497

Tian YH, Feng Y, Gao W, 2025. Virtual modelling framework-based inverse study for the mechanical metamaterials with material nonlinearity. *Modelling*, 6(1):24. https://doi.org/10.3390/modelling6010024

Tong GS, 2022. Design Methods for Steel Structures and Steel–Concrete Composite Structures. China Architecture & Building Press, Beijing, China (in Chinese).

Tong JZ, Zhang JB, Tong GS, et al., 2022. Flexural tests and behavior of multi-celled corrugated-plate CFST members. *Journal of Building Engineering*, 49:104051. https://doi.org/10.1016/j.jobe.2022.104051

Tong JZ, Wu RM, Wang LQ, 2023a. Experimental and numerical investigations on seismic behavior of stiffened corrugated steel plate shear walls. *Earthquake Engineering & Structural Dynamics*, 52(12):3551-3574. https://doi.org/10.1002/eqe.3920

Tong JZ, Wu RM, Xu ZY, et al., 2023b. Subassemblage tests on seismic behavior of double-corrugated-plate shear walls. *Engineering Structures*, 276:115341. https://doi.org/10.1016/j.engstruct.2022.115341

Tong JZ, Yu CQ, Tong GS, et al., 2023c. Experimental study on axial resistant behavior of multi-celled corrugated-plate CFST walls. *Engineering Structures*, 295:116795. https://doi.org/10.1016/j.engstruct.2023.116795

Tong JZ, Zhang JM, Yu CQ, et al., 2024a. Seismic experiments and shear resistance prediction of multi-celled corrugated-plate CFST walls. *Earthquake Engineering & Structural Dynamics*, 53(5):1681-1704. https://doi.org/10.1002/eqe.4091

Tong JZ, Wang LQ, Wu RM, et al., 2024b. Cyclic test and analysis of UHTCC-enhanced buckling-restrained steel plate shear walls. *Earthquake Engineering & Structural Dynamics*, 53(13):4006-4031. https://doi.org/10.1002/eqe.4212

Tong JZ, Zhang JM, Yu CQ, et al., 2024c. Experimental study on axial compressive behavior of concrete-filled corrugated steel tubular columns. *Engineering Structures*, 313:118267. https://doi.org/10.1016/j.engstruct.2024.118267

Tong JZ, Chen YL, Li QH, et al., 2025. Flexural performance and crack width prediction of steel-UHTCC composite bridge decks with wet joints. *Engineering Structures*, 323:119264. https://doi.org/10.1016/j.engstruct.2024.119264

Wang FC, Han LH, 2018. Analytical behavior of special-shaped CFST stub columns under axial compression. *Thin-Walled Structures*, 129:404-417. https://doi.org/10.1016/j.tws.2018.04.013

Wang WQ, Wang JF, Guo L, 2022. Mechanical behavior analysis of LEM-infilled cold-formed steel walls. *Sustainable Structures*, 2(1):000013. https://doi.org/10.54113/j.sust.2022.000013

Wen CB, Guo YL, Sun HJ, et al., 2023. Experimental and numerical study on seismic performance of concrete-infilled double steel corrugated-plate walls. *Journal of Building Engineering*, 68:106171. https://doi.org/10.1016/j.jobe.2023.106171

Wu RM, Wang LQ, Tong JZ, et al., 2024. Elastic buckling formulas of multi-stiffened corrugated steel plate shear walls. *Engineering Structures*, 300:117218. https://doi.org/10.1016/j.engstruct.2023.117218

Wu RM, Yu CQ, Wang LQ, et al., 2025. Shear elastic buckling of corrugated steel plate shear walls with stiffeners considering torsional rigidity. *Thin-Walled Structures*, 206:112646. https://doi.org/10.1016/j.tws.2024.112646

Yu CQ, Tong JZ, Tong GS, et al., 2023. Axial compressive performance and design of multi-celled corrugated-plate CFST walls. *Structures*, 57:105303. https://doi.org/10.1016/j.istruc.2023.105303

Yu CQ, Tong GS, Tong JZ, et al., 2024a. Experimental and numerical study on seismic performance of L-shaped multi-cellular CFST frames. *Journal of Constructional Steel Research*, 213:108360.

https://doi.org/10.1016/j.jcsr.2023.108360

Yu CQ, Tong JZ, Zhou SM, et al., 2024b. State-of-the-art review on steel–concrete composite walls. *Sustain Struct*, 4(1): 000035.
https://doi.org/10.54113/j.sust.2024.000035

Yu CQ, Tong JZ, Zhang JM, et al., 2025a. Axial compressive behavior of multi-celled corrugated-plate CFST walls: tests and numerical simulations. *Engineering Structures*, 322: 119033.
https://doi.org/10.1016/j.engstruct.2024.119033

Yu CQ, Duan SJ, Tong JZ, 2025b. Global buckling simulation and design of a novel concrete-filled corrugated steel tubular column. *Modelling*, 6(1):22.
https://doi.org/10.3390/modelling6010022

Yu M, Hu X, Xu LH, et al., 2022. A general unified method for calculating fire resistance of CFST columns considering various types of steel and concrete. *Journal of Building Engineering*, 59:105125.
https://doi.org/10.1016/j.jobe.2022.105125

Zhang JW, Tong JZ, Yu CQ, et al., 2023. Experimental evaluation on seismic performance of multi-celled corrugated-plate CFST walls. *Journal of Constructional Steel Research*, 201:107743.
https://doi.org/10.1016/j.jcsr.2022.107743

Zhang JM, Tong GS, Tong JZ, 2025. Global buckling prevention of multi-celled corrugated-plate CFST walls under pure in-plane bending loads. *Engineering Structures*, 332:120061.
https://doi.org/10.1016/j.engstruct.2025.120061

Zhang L, Yang SL, Fu B, et al., 2021a. Behavior and design of concrete-filled narrow rectangular steel tubular (CFNRST) stub columns under axial compression. *Journal of Building Engineering*, 37:102166.
https://doi.org/10.1016/j.jobe.2021.102166

Zhang L, Yang SL, Tong GS, et al., 2021b. Numerical analysis on concrete-filled wide rectangular steel tubular (CFWRST) stub columns under axial compression. *Structures*, 34:4715-4730.
https://doi.org/10.1016/j.istruc.2021.10.074

Zhang YJ, Tong GS, Tong JZ, et al., 2023. Experimental and numerical study on post-ultimate ductile performance of multi-celled concrete-filled steel tubular walls. *Journal of Constructional Steel Research*, 211:108097.
https://doi.org/10.1016/j.jcsr.2023.108097

Electronic supplementary materials

Section S1, Figs. S1–S4, Eqs. (S1)–(S50)